Methods

Sperm sample

Ejaculated spermatozoa were donated by Dr. Bo Harstine at Select Sires Inc. (bovine, Holstein) and Dr. Jie Xu at the University of Michigan (New Zealand rabbit) and purchased from Manhattan Cryobank and Fairfax Cryobank (human). Human sperm samples were acquired with approval from the University of Toledo's Institutional Review Board (IRB).

Preparation of sperm for study of asymmetric beating and frequency distribution

We used the swim-up technique to select motile bovine sperm for snap freezing. The swim-up technique was performed using the PureSperm Wash kit (Nidacon, PSW-100) as instructed. Briefly, one straw of cryopreserved bovine semen (0.5 mL; 40 x 10^6 sperm/mL) was thawed and placed in a round-bottom 15-mL tube. 1 mL of PureSperm wash solution (PSW-100) was placed on top of the semen. The tube was slanted at 45° and incubated at 37 °C for 1 hour. After incubation, the upper layer of approximately 1 mL was removed and placed in a new tube. The solution was monitored under a microscope for percent motility, and samples with more than 90% motile sperm were used for further processing. The collected upper layer was centrifuged at 250g for 20 min. The pellet was suspended in wash buffer (PSW-100) and centrifuged at 250g for 8 min. The pellet was resuspended in a minimal volume of Medium 199 (M4530) or PBS to concentrate the sperm. Approximately 15–20 µl of sample was placed on a glass slide, covered by cover glass, and immediately dropped into liquid nitrogen for snap freezing. Snap-frozen sample was processed for immunostaining as described in the Immunofluorescence section.

Study of asymmetric beating and occurrence distribution

The snap-frozen sperms were stained to locate the proximal centriole (PC) and distal centriole (DC) within the cells. The images were captured by randomly selecting varying fields of view. All cell images were rotated to produce a straight head and a head midline was drawn. The straight head sperm cells were oriented to place implantation fossa on left side and PC tip on the right side of the head midline. After that, the sperm cells were characterized as *slight right, straight, mild left, and sharp left*, based on the location of the tail and its direction of bending relative to the head midline. Cells were characterized as slight right when tail bending occurred at the sperm mid-piece and to the right of the midline. None of the cells displayed a kink at the neck when tail beating occurred to the right. Cells were characterized as straight when the head, mid-piece, and most of the principal piece were in line with the midline. Mild left cells displayed a mild kink at the neck or mild bending at the mid-piece to the left of the midline. Similarly, all sharp left cells showed a sharp kink at the neck and bending at the mid-piece. We further characterized mild left cells as Type 1 and Type 2, based on whether they showed a kink at the neck or bending at the mid-piece. Similarly, sharp left cells were characterized as Type 1 when there was a very sharp kink at the neck and Type 2 when there was a kink at the neck and a strong bend at the mid-piece.

Preparation of sperm for study by immunofluorescence

Motile ejaculated spermatozoa were selected by 40/80-density gradient using a PureSperm Wash kit (Nidacon, PS40-100, and PS80-100). A sperm pellet sample with at least 70–80% motility was used for further processing. The sperm pellet was resuspended in Medium 199 (Sigma Aldrich, M4530). Approximately 7 µL of cleaned spermatozoa were placed on a poly-lysine slide (Sigma-Aldrich, P5899), and a Sigmacote coverslip (Sigma, SL2) was placed on top. The entire slide was then snap frozen and stored in liquid nitrogen. Sperm slides were stored in liquid nitrogen until staining.

Preparation of sperm for STORM microscopy

For STORM imaging, motile sperm were selected by either density gradient or the swim-up technique. Motile sperm were placed on round cover glass (Fisher Scientific, 72231-01), allowed 5 minutes for movement around the cover glass, then fixed in prechilled (at -20 °C) methanol for 3 min. Then, the sample was prepared for immunostaining as described in the Immunofluorescence section. Alternatively, the selected sperm were placed on a MatTek glass-bottom dish (MatTek Corporation, P35G-1.5-10.C) and snap frozen in liquid nitrogen. The snap-frozen sperm were fixed in prechilled methanol for 3 min and prepared for immunostaining as described in the Immunofluorescence section.

Preparation of sperm for Cryo-ET

For cryo-EM, bovine semen was collected from Holstein bulls (CRV Delta, The Netherlands). Semen was diluted to a sperm concentration of ~30 x 10^6 cells/mL with either Tris-citrate buffer (96 mM Tris, 27 mM fructose, 35 mM sodium citrate, pH 7, 300 mOsm) or OptiXcell buffer (IMV technologies, 026218-025239). Sperm motility was assessed with a computer-assisted sperm analysis (CASA) system and found to be ~83% and ~85% for sperm diluted in Tris-citrate and OptiXcell, respectively. Sperm were diluted to a concentration of ~3 x 10^6 cells/mL. Approximately 3 µL of the sperm suspension was pipetted onto glow-discharged Quantifoil R 2/1 Holey carbon grids. One µL of a suspension of BSA-conjugated 10-nm gold beads (Aurion, 210.033) was added, and the grids were then blotted manually from the back (opposite the side of cell deposition) for ~3 s. Grids were immediately plunged into liquid ethane cooled to liquid nitrogen temperature and stored under liquid nitrogen until imaging.

Antibodies

Primary and secondary antibodies were purchased from various suppliers (**Table 1**). Concentrations of various antibodies used for confocal and STORM microscopy are listed in the table below:

Antibody	Confocal dilution	STORM dilution	Source and catalog number
FAM161A-S	1:300	1:100	Sigma Aldrich, #HPA032119
WDR90	1:100	1:20	Sigma Aldrich, #HPA061785
POC5	NA	1:80	Thermo Fisher Scientific, # PA5-84503
POC1B	NA	1:80	Thermo Fisher Scientific, # PA5-24495
CETN1 (2A6)	1:20	NA	Santa Cruz, # sc-293494
Beta Tubulin (E7)	NA	1:20	DSHB, AB_2315513
Anti-rabbitA647	1:300	1:100	Jackson Immunoresearch, #711-605-152
Anti-mouse647	1:300	1:100	Jackson Immunoresearch, #715-605-150
Anit-mouse488	1:200	NA	Jackson Immunoresearch,# 715-545-150

Table 1: Antibodies used in this study, NA – not applicable

Immunofluorescence

For staining, slides were removed from liquid nitrogen, the coverslip was removed using forceps, and the slide was placed in a pre-chilled Coplin jar of ice-cold methanol for 3 min. Next, the slide was placed in phosphate-buffered saline (PBS) for 1 min, then set for 60 min in fresh PBS with 0.3% Triton X-1000 (PBST) at room temperature. PBST-B was prepared by adding 1% bovine serum albumin (BSA) to PBST and slides were then placed in PBST-B for 30 min. Primary antibodies diluted in PBST-B were added to the slides, after which the slides were covered in parafilm, placed in a humidity chamber, and incubated overnight at 4 °C. The slides were washed three times in PBST for 5 min each. Next, the secondary antibody mixture was prepared by adding secondary antibody and Hoechst (#H3569, Thermofisher Scientific, 1:200) to PBST-B solution. The secondary antibody mixture was added to the slides, which were then covered in parafilm and incubated for 2 h at room temperature. Slides were then washed three times with PBST for 5 min each, followed by three washes with PBS for 5 min each.

For STORM imaging, immunostaining protocol was followed as described above with slight modification. Incubation in primary antibody was done for 24 hours at 4 °C, and incubation in secondary antibody was done for 4 hours at room temperature. Washes after primary and secondary antibody incubations were completed 5 times for five minutes with each solution. After washes, the cover glass or MatTek dishes were stored in PBS at 4 °C. Imaging was performed within 24–48 hours.

Confocal imaging

Slides were sealed and imaged using a Leica Sp8 confocal microscope, and some images were processed using a Leica HyVolution 2 System. Images of sperm were captured at a magnification of 63X and a zoom of 6X, with 512 × 512 pixel density. Using Photoshop, immunofluorescence sperm images were cropped to 200 × 200 pixels or 65 × 65 pixels. The overall intensity of the images was modified to allow easy visualization, and panels were resized to 1 × 1 inch and 300 DPI for publication.

STORM microscopy

3D STORM imaging was performed on a Nikon N-STORM4.0 system using an Eclipse Ti inverted microscope, an Apo TIRF 100× SA NA 1.49 Plan Apo oil objective, 405-, 561-, 488-, and 647-nm excitation laser line (Agilent), and a back-illuminated EMCCD camera (Andor, DU897). The 647-nm laser line was used to promote fluorophore blinking. A 405-nm laser was used to reactivate fluorophores. ~30,000 time points were acquired at a 20 Hz frame rate, each 16–20 ms in duration. NIS-Elements (Nikon) was used to analyze and present the data. For imaging samples on cover glass, the cover glasses were mounted on a depression slide in imaging buffer (10% dextrose in 100 mM Tris at pH 8.0, 25 mM β-Mercapto-ethylamine, 0.5 mg/mL glucose oxidase, and 67 µg/mL catalase). The cover glass was sealed with Body Double SLK (SO56440A and SO5644B) and allowed 3 minutes to air dry, after which the sample was processed for imaging. For imaging samples on a MatTek Dish, 1 mL of imaging buffer was placed into the dish and imaged under the STORM microscope.

The raw data obtained by image acquisition for all STORM images was analyzed using NIS-Elements. Analyzed images were exported in TIF format. Publication-ready STORM images were prepared in Photoshop by cropping to 300 × 300, 100 × 100, or 65 × 65 pixel sizes and resizing cropped images to 1 × 1 inch and 300 DPI. The background intensity of the whole image was enhanced to clearly visualize the sperm head.

Cryo-electron tomography

Tilt series acquisition**.** Tilt series were acquired on a Talos Arctica (ThermoFisher) operated at 200 kV. The microscope was equipped with a post-column energy filter (Gatan) in zero-loss imaging mode with a 20-eV energy-selecting slit. All images were recorded on a K2 Summit direct electron detector (Gatan) in counting mode. Tilt series were collected using SerialEM (Mastronarde, 2005), with a Volta phase plate (VPP) [1], and at a target defocus of -0.75 µm. Tilt series were typically acquired in 2° increments over a range of ± 50° using a grouped dose-symmetric tilt scheme with groups of 3 tilts.

Tomogram reconstruction, segmentation, and analysis**.** Frames were aligned on-the-fly using Warp. Tomograms were reconstructed in IMOD (Tegunov and Cramer 2019 doi: 10.1038/s41592-019-0580-y) using weighted back-projection, with a SIRT-like filter (Zeng, 2012) applied for visualization and segmentation. VPP tomograms were not CTF-corrected. Segmentation was generally performed semi-automatically using the neural network-based workflow implemented in the TomoSeg package in EMAN 2.21 (Chen *et al*, 2017). Microtubules, however, were traced manually in IMOD. Segmentation was then manually refined in Chimera 1.12 (Pettersen *et al*, 2004). Visualization was performed in Chimera 1.12. Measurements were performed either in Fiji or in IMOD on central ~20-nm-thick slices through tomograms filtered with 20 iterations of a SIRT-like filter.

Intensity measurement by photon counting

For intensity measurements of the various proteins, images were captured using a confocal microscope in counting mode. All images were captured using a constant laser power of 5%. The images were then analyzed for protein intensity using the Leica LASx program. Briefly, a round region of interest (ROI) 1.5 µm in diameter was drawn to encompass the PC and DC, and pixel sum intensity was recorded for each ROI and exported into a Microsoft Excel sheet for additional calculations.

STORM image quantification

PC and DC dimension measurements: All measurements of STORM images were performed using Nikon's NIS-Elements imaging software. The accuracy of measurements in NIS-Elements was confirmed by measuring the diameter of the tubulin-stained sperm axoneme. Additionally, the resolutions of STORM and Cryo-ET were found to be comparable by measuring the dimensions of the tubulin-stained PC in STORM and microtubules observed in Cryo-ET imaging.

To measure rod length and width, a line, starting at 50% of the first intensity peak through 50% of the last intensity peak, was drawn and measured along the length and width of the rods.

Caudal and rostral distance measurements: Two distances (caudal and rostral) were measured for rod sliding analysis. Since the DC microtubules are connected to the axoneme, only their rostral distance was measured. Sperm cells were first rotated to make neck straight and were oriented to maintain the PC tip pointing to the right side, and bigger rod on left side of neck midline. This consistent reference was used for defining left-right rod and microtubules. Measurements were taken at the caudal and rostral ends of the right-side rod and microtubules relative to the left side rod and microtubules at the respective side. A measurement was assigned a "-ve" value when the right rod or microtubule was below the left rod or microtubules and a "+ve" value when the right side was above the left side.

Waveform amplitude $\bar{y}$, sliding $\bar{\Delta}$, and curvature $\bar{\kappa}$ of the sperm flagellum

We calculated three variables derived from the flagellum waveform to infer the "sliding filament" hypothesis during tail beating [2-7]: average flagellum beating amplitude ($\bar{y}$), microtubule sliding along the tail ($\bar{\Delta}$), and average waveform curvature ($\bar{\kappa}$). Importantly, the flagellum amplitude was measured relative to the sperm head orientation; however, curvature and microtubule sliding are quantities independent of head orientation.

The flagellar waveform was extracted with a semi-automated bespoke image processing algorithm in MATLAB to extract the coordinate values of every point along the flagellum relative to the sperm head $\boldsymbol{r}(s) = (\mathrm{x}(\mathrm{s}), \mathrm{y}(\mathrm{s}))$, parametrized by arclength s [2]. All flagellar shapes are rotated and translated so that the long axis of the sperm head is aligned with the x-axis, while the sperm neck is centered at the origin. The deflection of the tail shape in the y-direction thus captures the waveform's amplitude, with positive (negative) values for flagellar points laying on the right (left) in respect to the head. The right and left sides of the sperm head are determined by the conserved position of the proximal centriole, chosen here to always lean toward the head's right side. We refer to this as centriole orientation-based sperm analysis (COSA), as detailed in the Main Text. Average flagellar deviation from the x-axis along arc length is denoted by $\bar{y}$ and captures the average waveform deflection or amplitude relative to head orientation.

We consider a sliding filament model of the sperm flagellum for estimation of flagellar interfilament sliding [5]. The sliding filament model abstracts the flagellum using a two-dimensional representation composed of two filaments. Each constituent filament $\boldsymbol{r}_{\pm}(s) = \boldsymbol{r}(s) \pm \frac{a}{2}\hat{\boldsymbol{n}}(s)$ is separated by a distance a (flagellar diameter) normal to the flagellum centerline $\boldsymbol{r}(s)$ at every point in arclength s [2-7]. Geometry constrains the normal vector $\hat{\boldsymbol{n}}(s) = (-\sin\theta, \cos\theta)$ to the plane, where θ(s) is the angle between the fixed-frame x-axis and the tangent to the centerline $\hat{\boldsymbol{n}}(s) = \boldsymbol{r}_s$, where subscripts denote derivative in respect to s. Like a rail-track, the constituent filaments travel distinct contour lengths, forcing a geometrical arclength mismatch $\Delta_T - \Delta_0 = \Delta(s) = a(\theta(s) - \theta_0)$, where Δ_0 and θ_0 are the length mismatch and tangent angle, respectively, at $s = 0$. Δ_T is the total interfilament sliding along the flagellum, whilst $\Delta(s)$ captures the incongruence of interfilament sliding caused solely by waveform curvature, and thus in the absence of basal sliding Δ_0. This is referred to here as flagellar sliding $\Delta(s)$. From this, $\bar{\Delta}$ captures the average flagellar sliding along arclength. For the calculation of $\Delta(s)$, we took the flagellar diameter $a = 600\ \mathrm{nm}$. The signed waveform curvature is simply $\kappa(s) = \theta_s$, and $\bar{\kappa}$ denotes the average curvature along arclength.

Exploratory Factor Analysis (EFA)

The statistical grouping technique known as exploratory factor analysis (EFA) was utilized. First, s for consideration in the EFA was checked for normality. EFA combines variables into clusters based on their collinearity. These groupings can be further utilized to reduce the number of variables to be used as predictors in multivariable analyses. Highly correlated variables are combined to describe a factor. The 'loading' of these factors can be visualized as the Pearson correlation between each variable and its factor. The resulting factors are not collinear with each other and thus can be used together in multiple regressions. The varimax orthogonal rotation method was utilized. The Kaiser-Meyer-Olkin (KMO) measure of sampling adequacy was calculated (>0.5 indicates sample adequacy), and Bartlett's test of sphericity was used to assess matrix correlation between the variables using an alpha of 0.05 to indicate significant correlation. A scree plot was used to assess the number of factors in the model. EFA was carried out with a varimax rotation method. Variables were considered to make a significant contribution to their factor if their factor loadings were greater than 0.40.

Statistical analysis and reproducibility

All averages and standard deviations in this study were calculated in a Microsoft Excel Sheet. All correlations, regressions, t-test, and ANOVA analyses were performed using GraphPad Prism 8.0. The number of cells

analyzed (N) and all *P*-values are stated in each figure or figure legend. The *t*-test performed in this study is a two-tailed paired t-test. All quantification data are presented as Box and Whisker and scatter plots. All box and whisker plots are represented as minimum to maximum, showing all data points with medians and “+” signs marking the average. Each data point in all scatter plots represents a measurement for an individual cell. Unless otherwise noted, each experiment was performed at least three times. *P*-values are indicated as asterisks highlighting the significance of comparison: *$P<0.05$, **$P<0.01$, ***$P<0.001$, ****$P<0.0001$.

Supplementary Glossary, Figures, Video, and Legends

Glossary

Atypical Distal Centriole (DC): the centriole at the base of the sperm flagellum. It is located in the neck region and has an atypical architecture consisting of nine doublet microtubules splayed out around a pair of central singlets. The left and right microtubules are associated with a pair of centriole luminal proteins re-organized into rods. The central singlet microtubules are associated with a pair of electron-dense bars.

Basal Body: a synonym for a centriole attached to the base of the axoneme. Here, the DC is a basal body.

Basal Sliding: sliding of the DC microtubules at the base of the axoneme near the sperm head.

Basal sliding displacement: the basal sliding amplitude between the rostral or caudal ends of the left and right DC rods and microtubules.

Centriole: a cylinder-like subcellular structure that forms centrosomes, cilia, and flagella. When found at the base of cilia and flagella, also known as the basal body. Canonical centrioles consist of triplet microtubules arranged symmetrically around a luminal scaffold. The luminal scaffold, together with linkers between triplets, maintains the rigidity of canonical centrioles.

Centriole orientation-based sperm analysis (COSA): The orientation of sperm images based on asymmetry of implantation fossa location, PC tip direction, DC rods size, or SCs shape.

Dynamic Basal Complex (DBC): Multiple components in the neck, which includes the distal centriole (DC), the proximal centriole (PC), and the striated columns (SC). The DC and SCs are continuous distally with axoneme and outer dense fibers (ODFs), respectively. The DC and SCs are continuous rostrally with the PC and capitulum, which connects to the base plate, which in turn is linked to the nuclear envelope.

Head Kink Angle: the angle formed between the head midline (long axis) and the neck midline when sperm beat asymmetrically to the left.

Head Kinking: the 2D head movement relative to the sperm long axis.

Head Twitching: change in head attachment angle to the neck, or change in head-neck angle during sperm movement; can be described as head pivoting or head orientation change relative to neck orientation.

Implantation Fossa: A head depression at the nucleus base where the tail is connected.

Sperm Neck: also known as the connecting piece or head-tail coupling apparatus (HTCA), the sperm neck region connects the head and axoneme tail and flagellar ultrastructure.

Sperm rolling: sperm head rotation around its swimming direction.

Sperm lateral displacement: sperm 3D corkscrew-like movement result in a 2D side-to-side movement along its swimming direction.

Sliding filament hypothesis: a model that explains the flagellar bending movement as a result of up-and-down parallel sliding movements of the axonemal microtubules relative to each other.

Tail Beating: tail bending that generates the force required to move sperm.

Canonical Centriole: a centriole with typical classical structure, found in most cell types; the PC in the sperm. It has nine-fold triplet interconnected microtubules, an overall cylindrical shape, and is radially symmetrical.

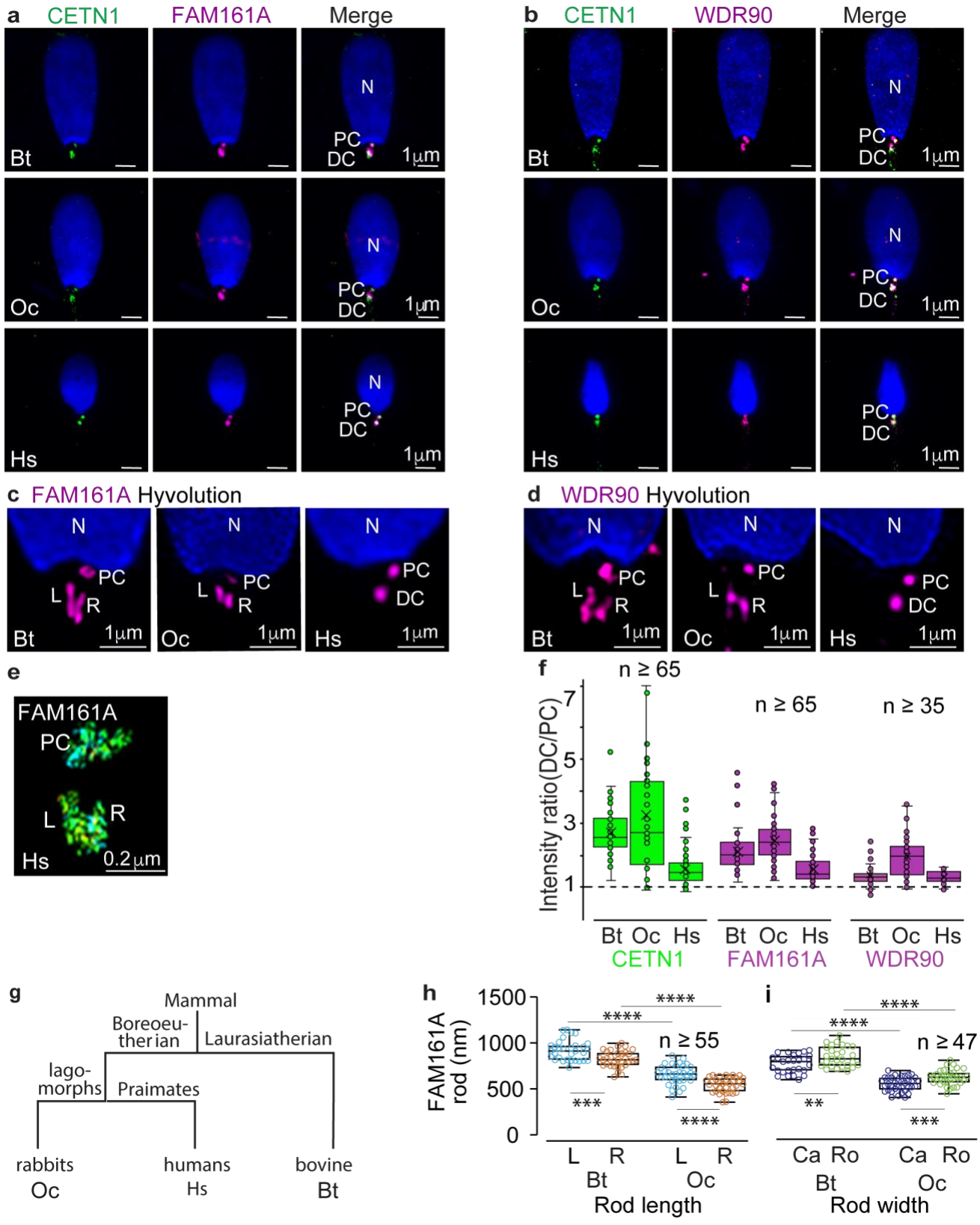
a CETN1 FAM161A Merge
b CETN1 WDR90 Merge
N
PC
DC
Bt
Oc
Hs
1μm
c FAM161A Hyvolution
d WDR90 Hyvolution
L
R
e
FAM161A
0.2μm
f
n ≥ 65
n ≥ 65
n ≥ 35
Intensity ratio(DC/PC)
CETN1
FAM161A
WDR90
g
Mammal
Boreoeu-therian
Laurasiatherian
lago-morphs
Praimates
rabbits
humans
bovine
h
FAM161A rod (nm)
n ≥ 55
Rod length
i
n ≥ 47
Rod width
Ca
Ro

Extended Data Fig. 1: FAM161A and WDR90 are novel proteins in the atypical distal centriole.

a–b) FAM161A (**a**) and WDR90 (**b**) colocalize with CETN1 at the PC and DC in spermatozoa of bovines (Bt), rabbits (Oc), and humans (Hs).

c–d) In bovine and rabbit spermatozoa**,** FAM161A (**c**) and WDR90 (**d**) appear as two rods by HyVolution. In human spermatozoa, they appear as dots.

e) STORM imaging of human sperm shows two rods of FAM161A at the DC**.** Note: STORM reflects labeling distribution, not intensity.

f) CETN1, FAM161A, and WDR90 are enriched in the distal centriole of spermatozoa.

g) Bovines (Laurasiatherian), humans (Boreoeutherian; Primates), and rabbits (Boreoeutherian; lagomorphs) represent three major phylogenetic groups of mammals.

h–i) FAM161A-labeled rods have species-specific sizes. The measurements are based on confocal HyVolution imaging. L, left; R, right; $^{**}P<0.01$, $^{***}P<0.001$, $^{****}P<0.0001$; ns, not significant

a

PC microtubules	STORM	n	Cryo-ET	n	P
Base (nm)	252±23	27	253±16	20	0.9
Tip (nm)	236±31	27	229±19	20	0.5
Axoneme (nm)	211±27	27			

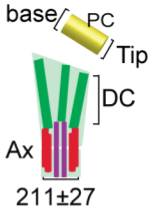

b

	Rods	n	Bars	n	P
Angle	12±3	30	5±6	20	<0.0001

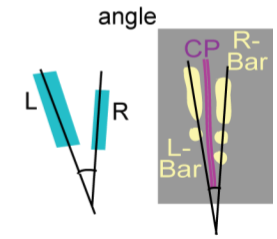

c

	POC5 Rods	n	Bars	n	P
The external edge to edge gap (nm)	280±31	30	195±27	20	<0.0001

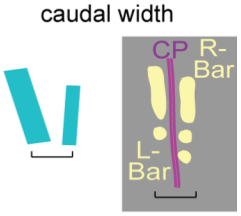

d

	L Bars	n	R Bars	n	P
Number of plates	1.5±0.61	20	2.2±0.77	20	0.003
Overall length (nm)	435±60	20	500±124	20	0.05
Distance to same side microtubule (nm)	171±26	13	105±25	13	<0.0001

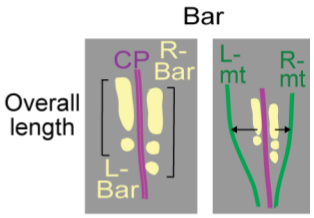

e Statistal analysis (p values)

rods/mts.	left rod vs right rod length	left rod vs right rod width
POC5	3E-05	6E-05
POC1B	2E-14	1E-24
FAM161A	9E-57	2E-08
Tubulin	0.02	

Extended Data Fig. 2: Rods and bars show distinct organization inside the DC.

a) Measurement of PC size based on STORM imaging with tubulin staining and measurement of PC microtubule diameter based on cryo-ET imaging shows that the observations from the two techniques are consistent.

b) Rods show a V-shape orientation, and bars show almost parallel orientation. Comparison of angles between POC5 L-R rods and bars.

c) Bars are distinct from rods and are located interiorly to the rods. POC5 rod and bar width at the caudal end.

d) Number of plates in left (L) and right (R) bars, overall length of L-R bars, and L-R bar distance from respective side microtubules. L-mt, Left microtubules; R-mt, Right microtubules; L-Bar, left bars; R-Bar, right bars.

e) Statistical analysis between L-R rods of various proteins. All measurements are shown in Fig. 1b–e.

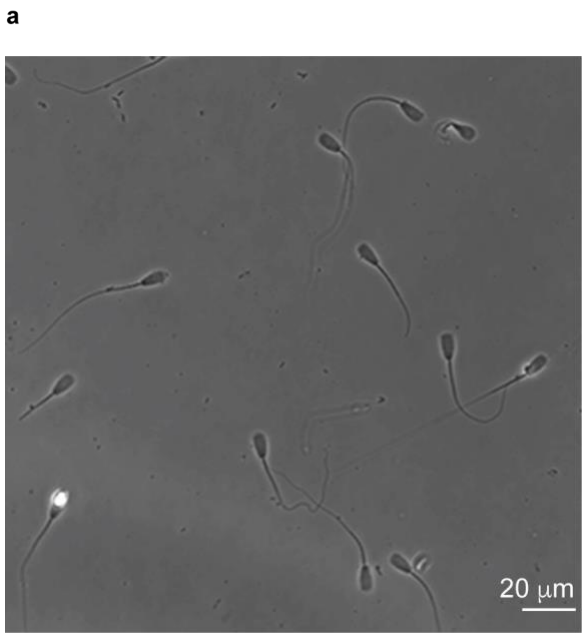

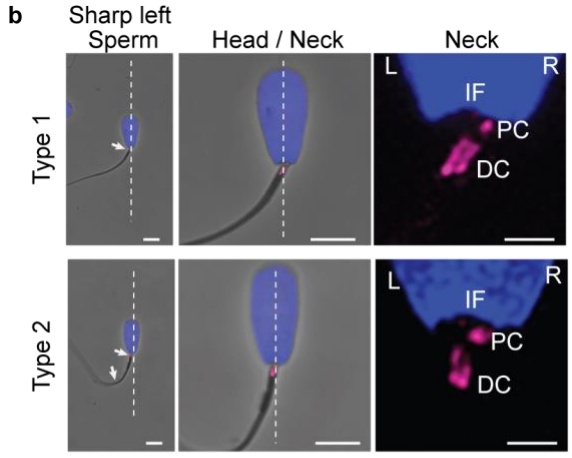

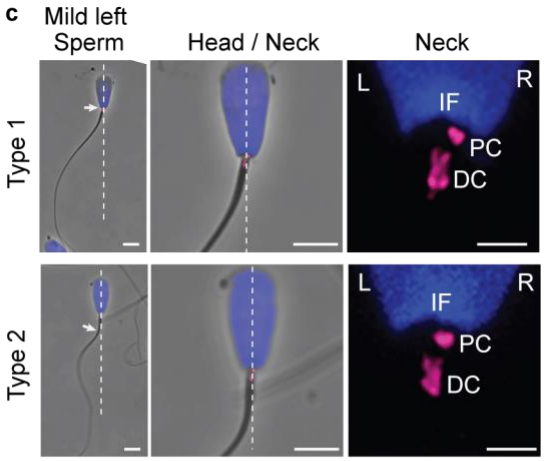

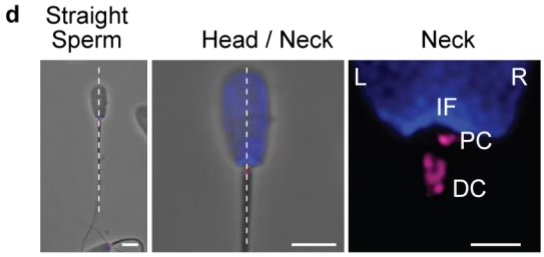

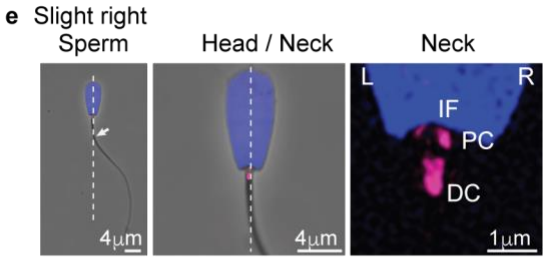

f

Exp #, n	Sharp left	Mild left	Straight	Slight right	Sharp right
1, 80	11	23	29	17	0
2, 51	8	13	20	10	0
3, 69	9	23	25	12	0
4, 48	9	15	16	8	0
% of total, 248	15	30	36	19	0
			*		
			****		

Extended Data Fig. 3: Sperm tail beating is biased towards the left side.

a) Low magnification phase image showing varying types of sperm tail beating in snap-frozen sperm cells.

b–e) Images showing sharp left sperm cells **(b)**, mild left **(c)**, straight **(d)**, and slight right cells **(e)**. The first panel shows a low magnification whole sperm cell with a straight head and direction of tail beating relative to the head midline. The second panel shows a zoom-in of the head and neck, and the third panel shows a zoom-in of the neck emphasizing implantation fossa and PC at the right side of sperm cells. The two types in **(b)** and **(c)** are subgroups of sperm that have been characterized based on tail bending location. The white arrowhead marks the tail bending position. The white dotted line marks the head-neck midline. The arrow marks the location of tail bending. L: left, R: right, IF: Implantation fossa

f) Table summarizing four experiments, each carried out with 48-80 sperms, (n) that found the percentage of sperm in each category of tail curvature. *P<0.05, ****P<0.0001

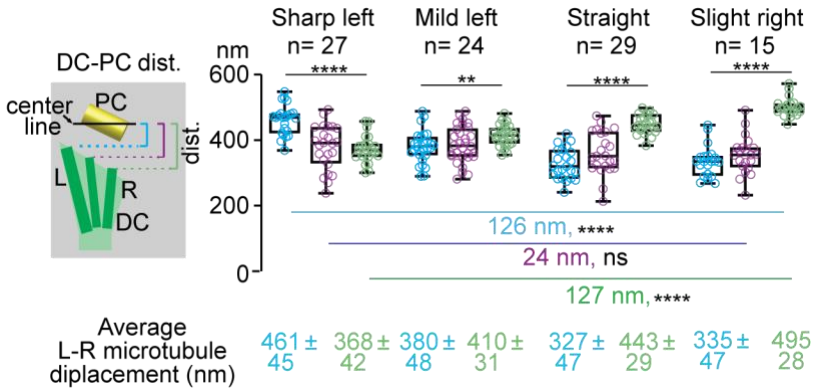

Extended Data Fig. 4: DC central microtubules are relatively more stable than left- and right-side microtubules.

Measurements showing distance between the PC central line (marked by black line) and DC left-, central-, and right-side microtubules. The average L-R microtubule displacement shows the mean ± standard deviation distance (dist.) between the PC centerline and L-R microtubules in four different groups of sperm cells. ***P*<0.01, *****P*<0.0001; ns, not significant.

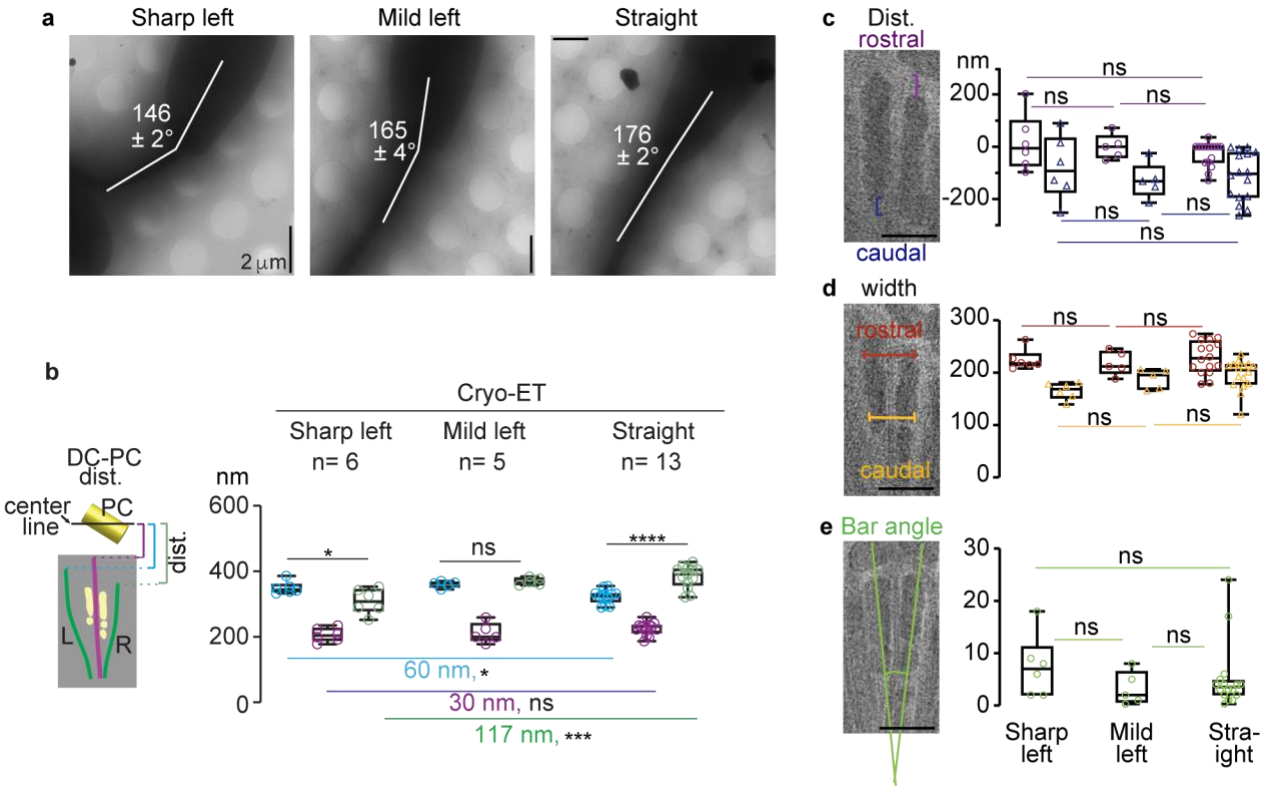

Extended Data Fig. 5: The bars are relatively stable during sperm tail beating.

a) Low-magnification cryo-EM projection images of bovine sperm, showing head-neck angles in three different groups of cells

b) Measurements showing the distance (dist.) between PC centerline and left-, central-, and right-side microtubules, based on cryo-ET imaging. **P*<0.05, ****P*<0.001, *****P*<0.0001, ns, not significant

c–e) No significant difference is detected between sharp left and straight sperm cells, which includes measurements of the rostral and caudal distance of bars (**c**), the width between the bars (**d**), and the angle between the bars (**e**). The measurement scheme is shown in the figures at the left side of each graph. The Y-axis shows various measurements, and the X-axis shows the various groups of cells, categorized based on tail bending. Scale bars (**c-e**), 0.25 μm. ns, not significant.

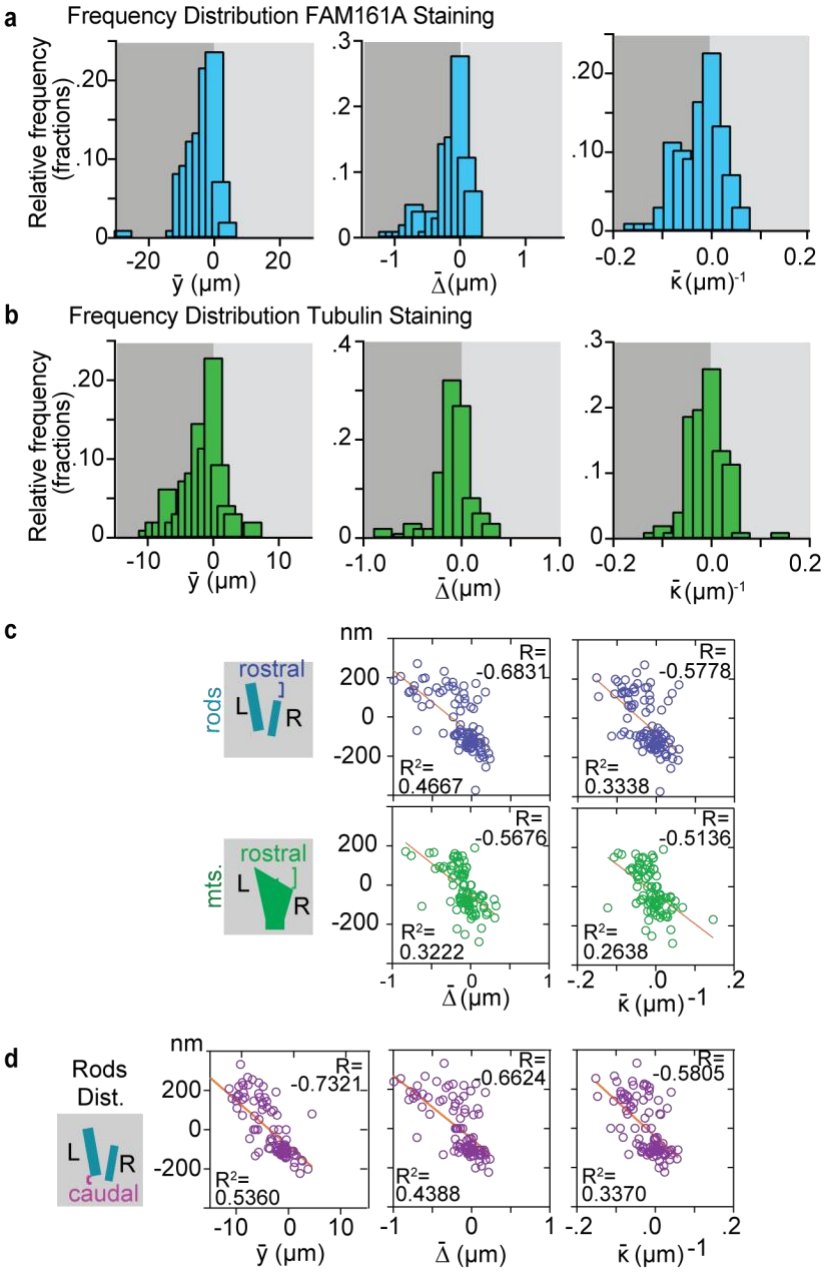

Extended Data Fig. 6: Tail beating is biased to the left and is correlated with the DC's internal sliding.

a–b) Sperm tail beating is skewed towards the left side**.** Histogram plot showing distributions of average amplitude, $\bar{y}$ (μm), of tail beating, microtubule sliding, $\bar{\Delta}$(μm), and curvatures, $\bar{\kappa}$ (μm) $^{-1}$, measured with FAM161A **(a)** and tubulin **(b)** staining. The dark and light shadow depicts the left and right sides of the tail beating with all three variables ($\bar{\Delta}$, $\bar{\kappa}$, $\bar{y}$).

c) The change in rod and microtubule rostral distance during sperm tail beating correlates with tail variables ($\bar{\kappa}$, $\bar{y}$).

d) The change in rod distance at the caudal end during sperm tail beating correlates with all three tail variables ($\bar{\Delta}$, $\bar{\kappa}$, $\bar{y}$).

Statistics of all correlation analysis is ****P<0.0001

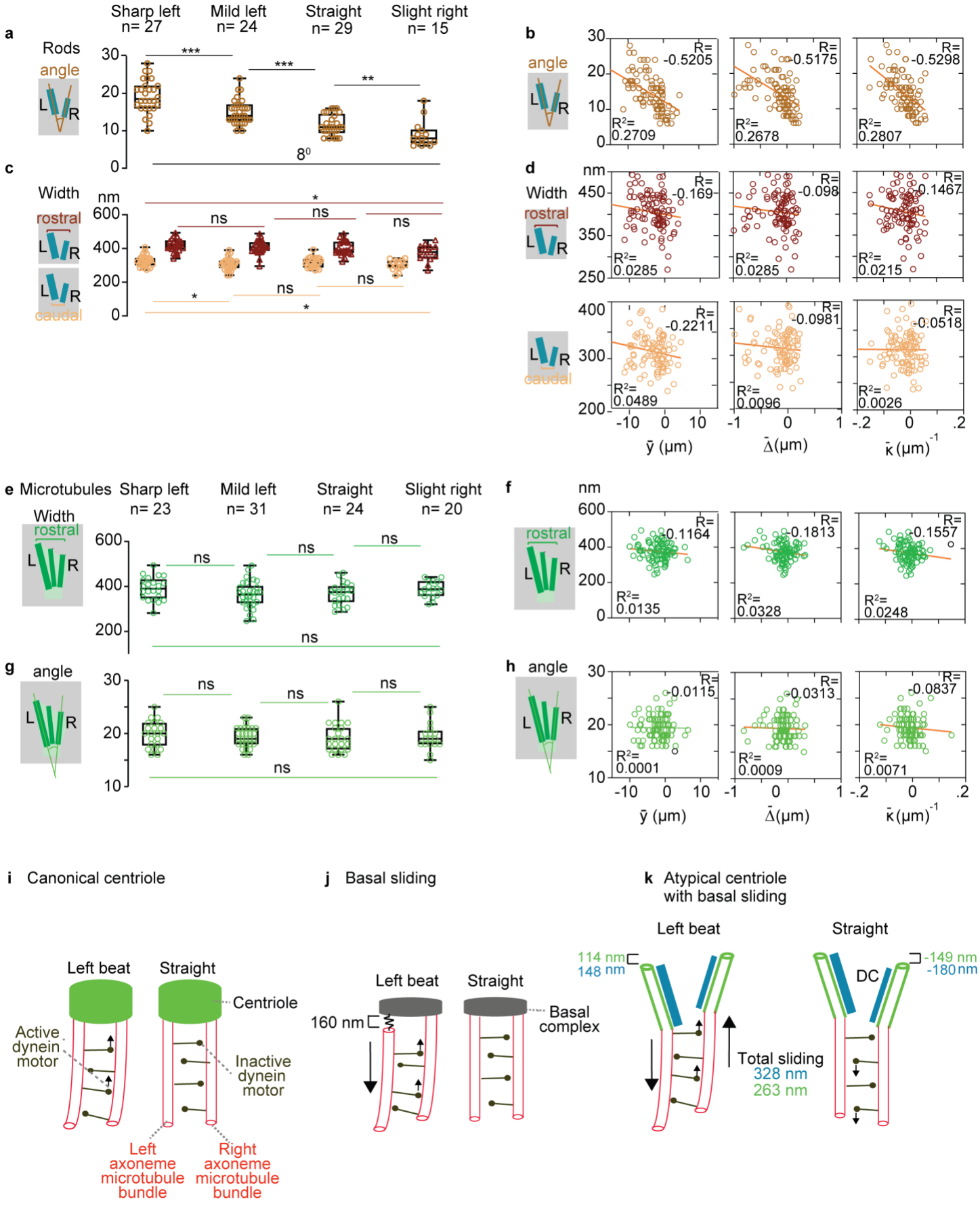
a
Sharp left
n= 27
Mild left
n= 24
Straight
n= 29
Slight right
n= 15
Rods
angle
L
R
***
***
**
8⁰
c
Width
nm
rostral
caudal
ns
*
b
angle
R= -0.5205
R²= 0.2709
R= -0.5175
R²= 0.2678
R= -0.5298
R²= 0.2807
d
Width
rostral
caudal
R= -0.169
R²= 0.0285
R= -0.098
R²= 0.0285
R= 0.1467
R²= 0.0215
R= -0.2211
R²= 0.0489
R= -0.0981
R²= 0.0096
R= -0.0518
R²= 0.0026
ȳ (μm)
Δ̄(μm)
κ̄ (μm)⁻¹
e Microtubules
Sharp left
n= 23
Mild left
n= 31
Straight
n= 24
Slight right
n= 20
Width
rostral
g
angle
f
rostral
R= 0.1164
R²= 0.0135
R= 0.1813
R²= 0.0328
R= 0.1557
R²= 0.0248
h
angle
R= 0.0115
R²= 0.0001
R= 0.0313
R²= 0.0009
R= 0.0837
R²= 0.0071
i Canonical centriole
Left beat
Straight
Centriole
Active dynein motor
Inactive dynein motor
Left axoneme microtubule bundle
Right axoneme microtubule bundle
j Basal sliding
Left beat
Straight
160 nm
Basal complex
k Atypical centriole with basal sliding
Left beat
Straight
114 nm
148 nm
DC
-149 nm
-180 nm
Total sliding
328 nm
263 nm

Extended Data Fig. 7: The geometric clutch hypothesis may not be acting during sperm tail beating.

Correlation was undetected between the microtubule angle and the flagellar waveform (**h**), indicating that "geometric clutch" effects may be absent at the DC [7].

a-b) Measurement of rod angle during sperm tail beating **(a)** and correlation analysis with three tail variables ($\bar{\Delta}$, $\bar{\kappa}$, $\bar{y}$) **(b)**. Statistics of correlation analysis, ****p<0.0001.

c-d) Measurement of rod rostral and caudal width **(c)** during sperm tail beating and correlation analysis with tail parameters **(d)**. *P<0.05; ns, not significant.

e-h) Measurement of microtubule rostral width **(e)** and correlation analysis with tail variables **(f).** Microtubular angle measurement **(g)** and correlation analysis **(h)**

i) Schematic representation of the classical model of axoneme sliding movement without sliding at the base upon flagellar bending; i.e., the microtubules are cemented at the base.

j) Schematic representation of the basal sliding model, including predicted basal sliding displacement (black arrow) of 160 nm in bovine sperm from the most widely accepted motor-control hypothesis [6].

k) Schematic representation of the dynamic basal complex, showing its constituent microtubules and rods sliding bidirectionally at the base end between sharp left to slight right beating.

Correlation analysis in Fig **7d**, **f**, and **h** are not significant (ns)

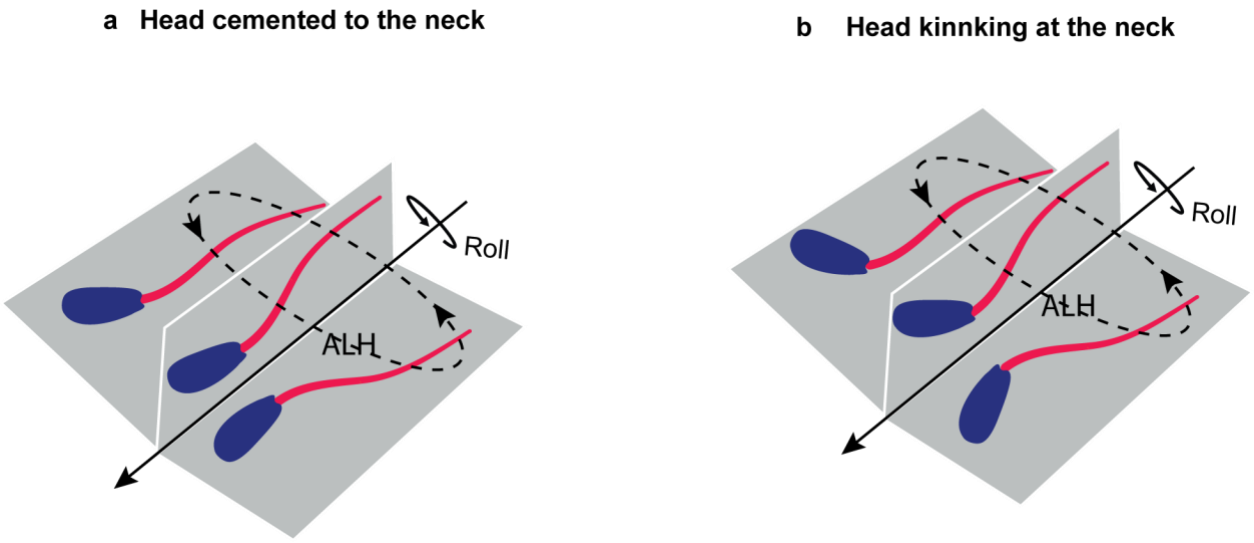

Extended Data Fig. 8: Types of sperm head motion: rolling, lateral displacement, and kinking.

A putative depiction of sperm movement with a head cemented to the neck (**a**) and sperm movement with a head movement relative to the neck (**b**). The spiral movement of spermatozoa swimming through a medium includes two previously described types of movements – rolling and lateral displacement (**a**) – as well as a third type that we have discovered in this study: kinking (**b**). Rolling is the rotational movement of spermatozoa around their long axis [8-10]. The rolling is due to the three-dimensional component of the beat of the flagellum. Lateral displacement is the two-dimensional appearance of circular motion of spermatozoa along their swimming path. Kinking is the back-and-forth motion of the spermatozoan head during sperm tail beating. ALH, amplitude of lateral head displacement.

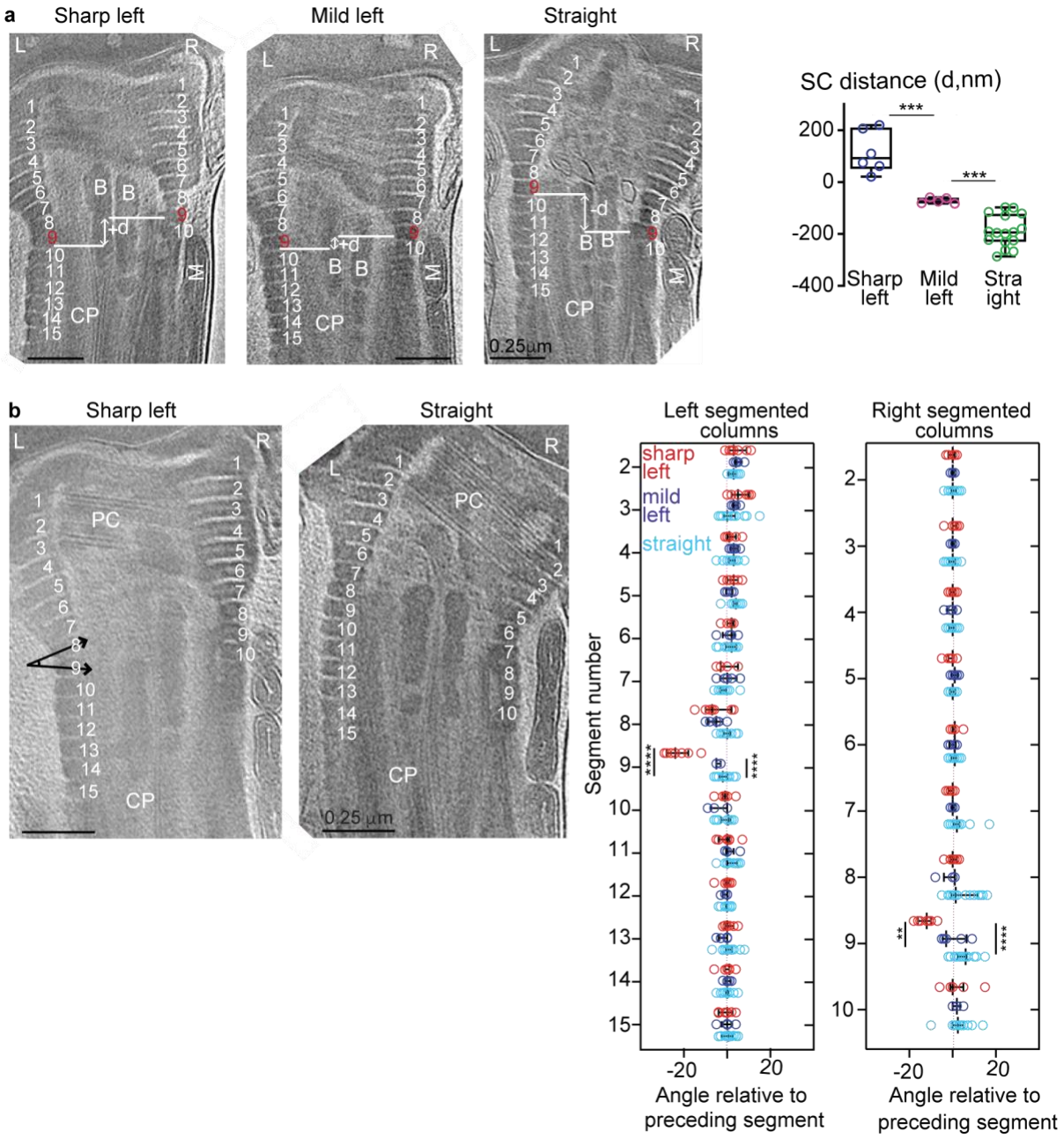

Extended Data Fig. 9: Striated columns slide during sperm tail beating.

a) Slices through VPP cryo-tomograms of three groups of sperm. Segmented columns are labeled and numbered based on the convention used for measurements. The plot on the right shows the relative distance (d) between a fixed segment (segment 9) in the left segmented columns and its corresponding segment in the right segmented columns. Negative values indicate that segment 9 on the right was lower than segment 9 on the left ("-d"), while positive values indicate that segment 9 on the right was higher than segment 9 on the left ("+d"). Every data point represents a cell, and lines represent mean ± standard deviation.

b) Relative angles between each segment were measured as shown in the two left panels. Every data point represents a cell, and lines represent mean ± standard deviation. $^{**}P<0.01$,$^{****}P<0.0001$

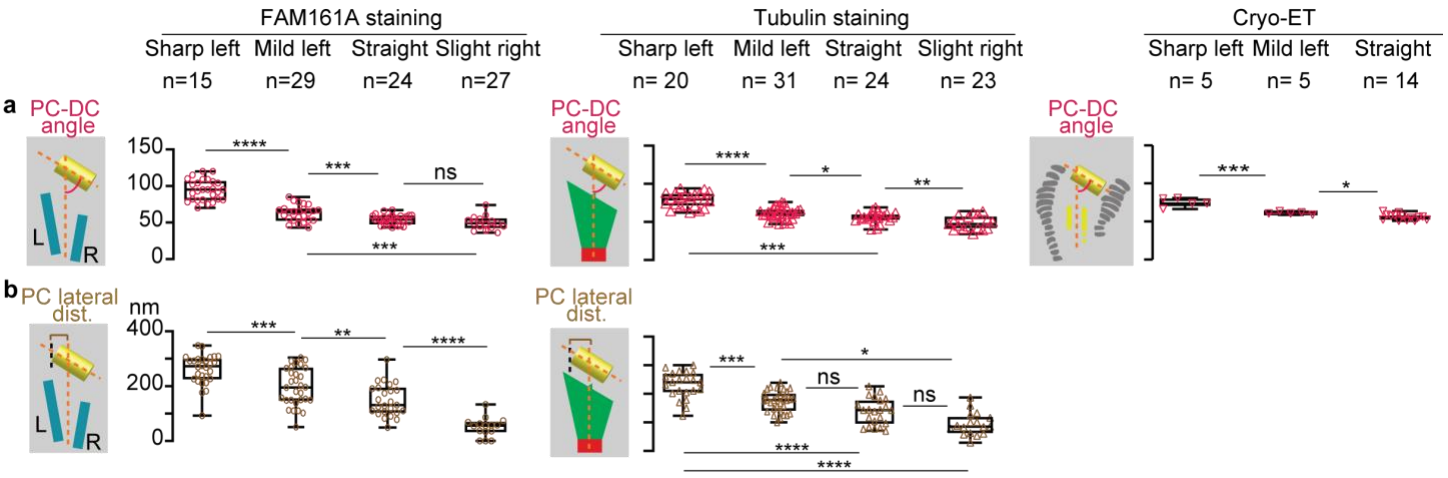

Extended Data Fig. 10: PC position changes during sperm tail beating.

a) The angle of the PC relative to the neck midline changes as the sperm tail bends from sharp left to right, shown based on STORM (left two panels) with FAM161A and tubulin staining and Cryo-ET (right panel). The angle between PC and neck midline was measured.

b) The PC changes its lateral position relative to the neck midline as the sperm tail bends from sharp left to right, shown based on STORM imaging with FAM161A and tubulin staining. The lateral distance was measured between neck midline and the left edge of the PC. **P*<0.05, ***P*<0.01,****P*<0.001,*****P*<0.0001, ns, not significant.

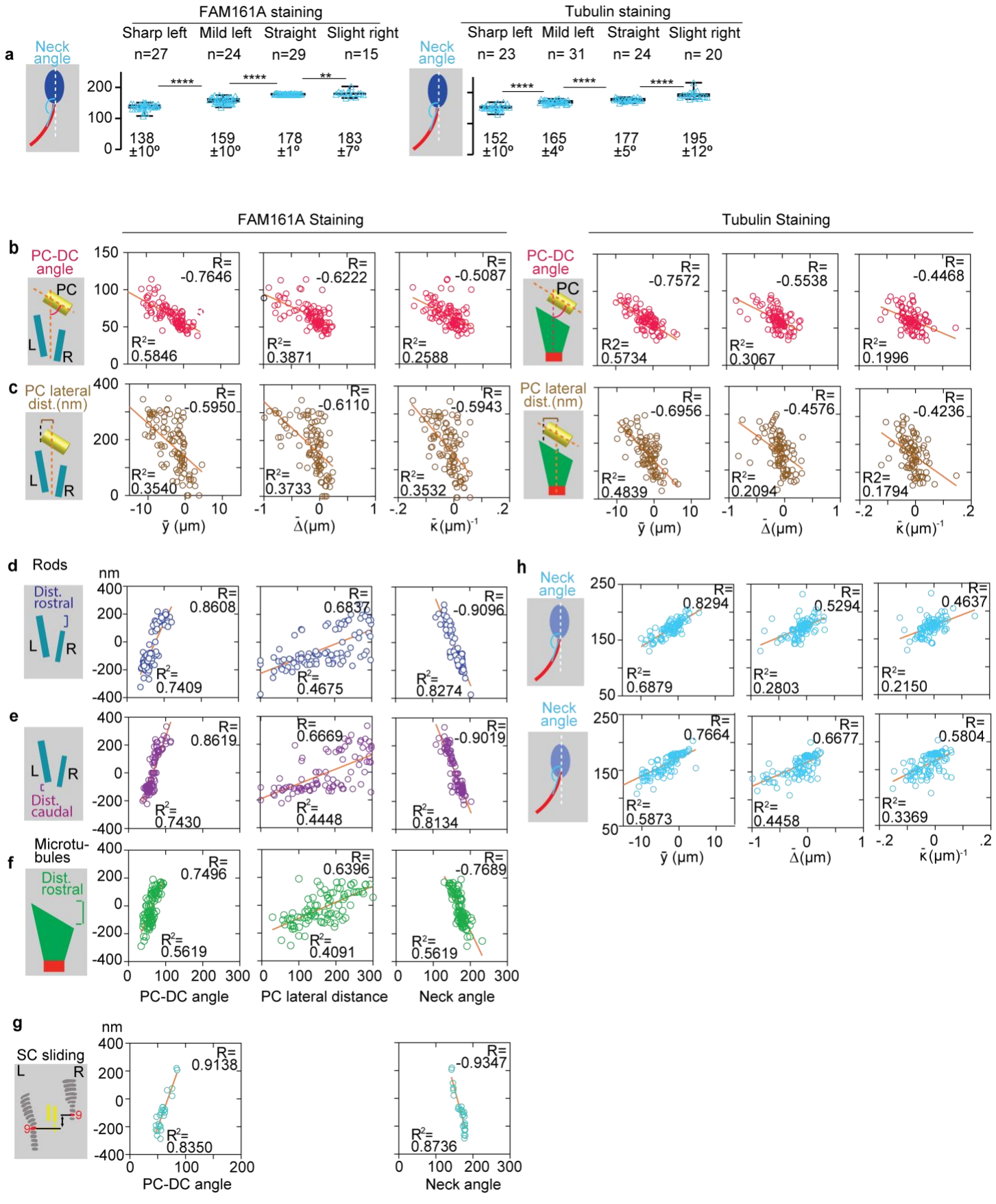
a
FAM161A staining
Sharp left
Mild left
Straight
Slight right
n=27
n=24
n=29
n=15
Neck angle
138 ±10°
159 ±10°
178 ±1°
183 ±7°
Tubulin staining
n= 23
n= 31
n= 24
n= 20
152 ±10°
165 ±4°
177 ±5°
195 ±12°
b
FAM161A Staining
Tubulin Staining
PC-DC angle
PC
L
R
R= -0.7646
R²= 0.5846
R= -0.6222
R²= 0.3871
R= -0.5087
R²= 0.2588
R= -0.7572
R2= 0.5734
R= -0.5538
R²= 0.3067
R= -0.4468
R²= 0.1996
c
PC lateral dist.(nm)
R= -0.5950
R²= 0.3540
R= -0.6110
R²= 0.3733
R= -0.5943
R²= 0.3532
R= -0.6956
R²= 0.4839
R= -0.4576
R²= 0.2094
R= -0.4236
R2= 0.1794
ȳ (μm)
Δ̄(μm)
κ̄(μm)⁻¹
d
Rods
Dist. rostral
nm
R= 0.8608
R²= 0.7409
R= 0.6837
R²= 0.4675
R= -0.9096
R²= 0.8274
e
Dist. caudal
R= 0.8619
R²= 0.7430
R= 0.6669
R²= 0.4448
R= -0.9019
R²= 0.8134
f
Microtu-bules
R= 0.7496
R²= 0.5619
R= 0.6396
R²= 0.4091
R= -0.7689
R²= 0.5619
PC-DC angle
PC lateral distance
Neck angle
g
SC sliding
R= 0.9138
R²= 0.8350
R= -0.9347
R²= 0.8736
PC-DC angle
Neck angle
h
Neck angle
R= 0.8294
R²= 0.6879
R= 0.5294
R²= 0.2803
R= 0.4637
R²= 0.2150
R= 0.7664
R²= 0.5873
R= 0.6677
R²= 0.4458
R= 0.5804
R²= 0.3369

Extended Data Fig. 11: Sperm tail beating correlates with PC and head position.

a) The head-neck angle changes as the sperm tail bends from sharp left to right, shown based on STORM with FAM161A (left) and tubulin (right) staining. The head-neck angle of each group is shown as mean ± standard deviation below the graph. ***P*<0.01,*****P*<0.0001

b–c) The change in PC-DC angle and PC lateral distance during sperm tail beating show high to strong correlation with tail variables ($\bar{\Delta}$, $\bar{\kappa}$, $\bar{y}$). The schematics shown to the left of each graph represent the measurements plotted on the Y-axis. All tail variables are plotted on the X-axis.

d–g) The change in PC-DC angle, PC lateral position, and head-neck angle correlate with rod sliding at the rostral end (**d**), rod sliding at the caudal end (**e**), microtubule sliding at the rostral end (**f**), and SC sliding (**g**).

h) The tail variables ($\bar{\Delta}$, $\bar{\kappa}$, $\bar{y}$) show a high to strong correlation with head-neck angle. Upper panel is with FAM161A staining and lower panel is with tubulin staining.
Statistics of correlation analysis, *****P*<0.0001

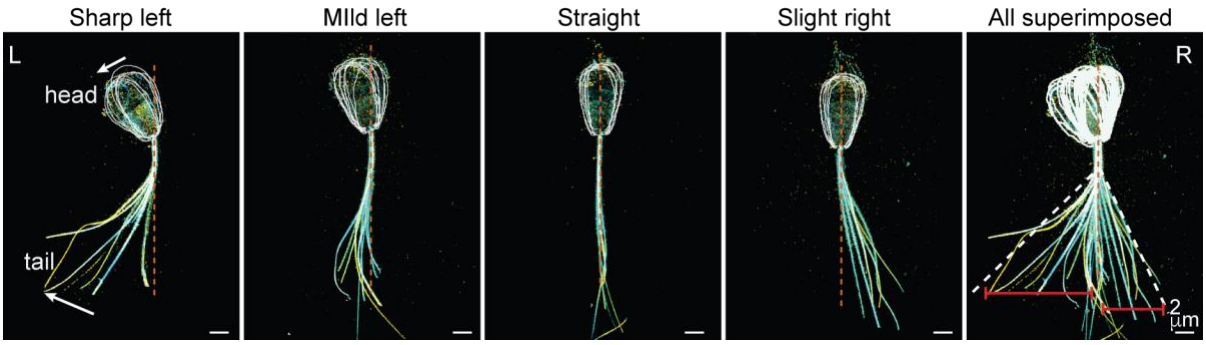

Extended Data Fig. 12: Head kinks sharp to the left when tail bends to the left.
Multiple cells from four different groups observed in 3D-STORM with tubulin staining. The staining was enhanced to visualize the head of the cells. The head is outlined with white line. Multiple cells with a range of curvature were selected for each group. The cells were aligned at the neck and superimposed together. The white arrow shows direction of head and tail bending. Orange dotted line marks the neck midline. The neck midline is not co-aligned with head and flagellum in sharp left cells. The red line in all superimposed cell marks the tail beating amplitude in left and right side relative to head.

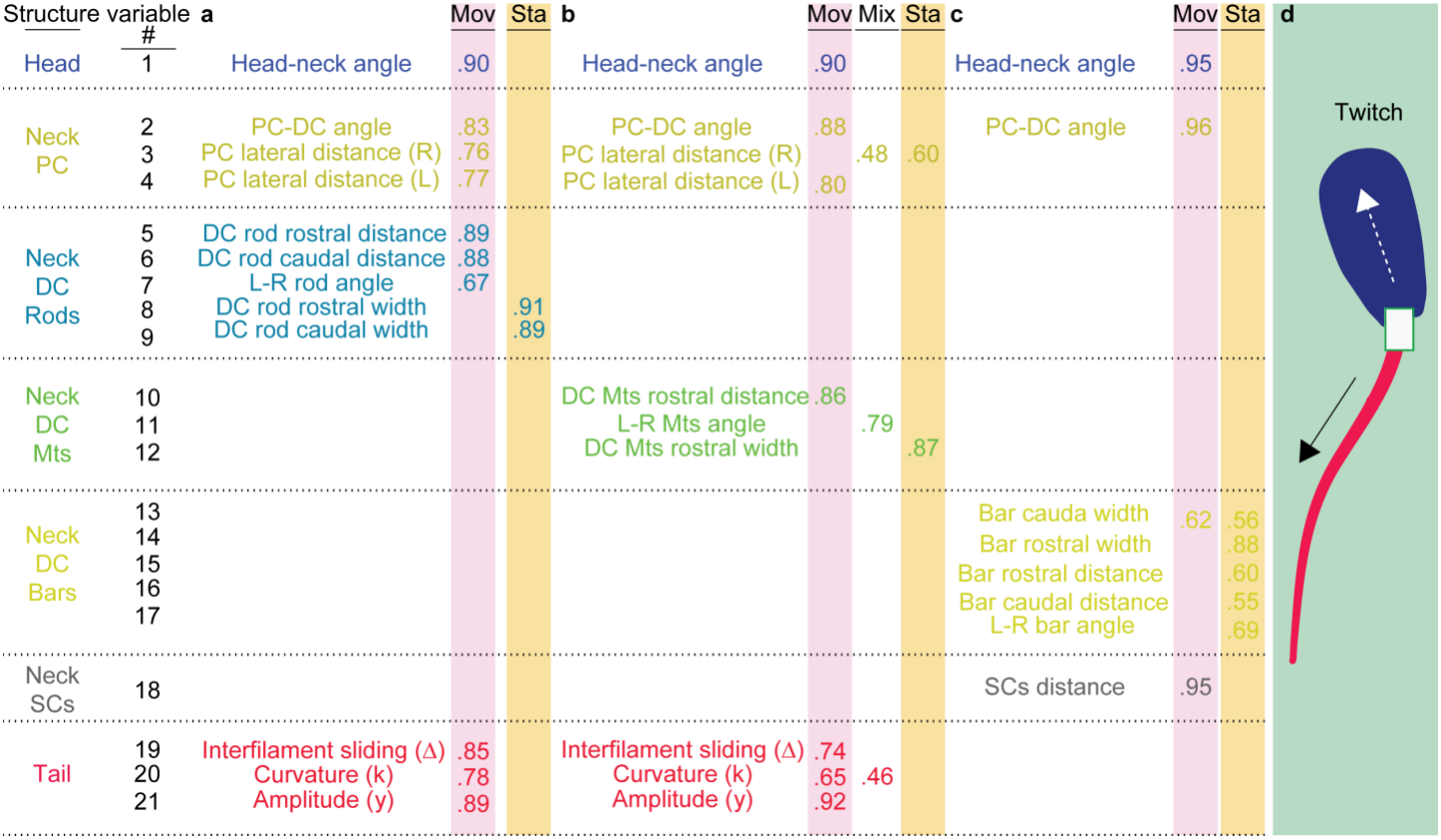

Extended Data Fig. 13: **The 21 sperm variables obtained from 3 data sets analyzed by Exploratory Factor Analysis (EFA).**

Three latent factors were identified: the tail-to-head coordinated movement (Mov) factor, the no movement of DC center and width (Sta) factor, and a mixture of the two (Mix) factor, suggesting a slight movement of some parts. Factor loadings are provided for each factor. Note that all factor loadings for both the Mov and Sta factors are above 0.5. Loadings (correlations) for each factor between variables is shown in column marked as Mov, Mix, and Sta.

a) A data set obtained by immunostaining for FAM161A and which included 97 sperm cells.

b) A data set obtained by immunostaining for tubulin and which included 93 sperm cells.

c) A data set obtained by cryo-EM and which included 21 sperm cells.

d) A sperm cell representing its various parts. EFA analysis shows coordinated movements of tail beating, neck deformation, and head kinking, resulting in a twitching movement.

Extended Data Video 1: Movie depicting modeling of straight, mild left, and sharp left cells, based on Cryo-ET imaging, as shown in Fig 3A.

Segmented columns are shown in transparent grey, the proximal centriole (PC) in green, distal centriole (DC) doublets in blue, distal centriole singlets in pink, the left bar in yellow, and the right bar in orange. Note the tilting deformation of the connecting piece as well as the upward sliding of the right segmented columns. Also note how this motion causes the PC to tilt towards the DC and to shift laterally towards the DC centerline.

Extended Data Video 2: **Movie depicting** putative **tail and head bending in sharp left to slight right sperm cells.**

The still images aligned at straight neck were played as video to depict the head and tail bending from sharp left to slight right cells based on 3D-STORM and tubulin staining. Multiple cells were selected based on the curvature (higher to lower for sharp left – straight and lower to higher for slight right cells) from each group. Head is outlined with white line and the dotted orange line depicts the neck midline. Scale bar 2 μm.

References

1 Danev, R. Cryo-EM single particle analysis with the Volta phase plate. Elife. doi: 10.7554/eLife. 13046.001 Danev R, Buijsse B, Khoshouei M, Plitzko JM, Baumeister W (2014) Volta potential phase plate for in-focus phase contrast transmission electron microscopy. *Proc Natl Acad Sci USA* **111**, 15635-15640 (2016).

2 Gadelha, H., Gaffney, E. A. & Goriely, A. The counterbend phenomenon in flagellar axonemes and cross-linked filament bundles. *Proc Natl Acad Sci U S A* **110**, 12180-12185, doi:10.1073/pnas.1302113110 (2013).

3 Gadêlha, H. The filament-bundle elastica. *IMA Journal of Applied Mathematics* **83**, 634-654, doi:10.1093/imamat/hxy011 (2018).

4 Coy, R. & Gadêlha, H. The counterbend dynamics of cross-linked filament bundles and flagella. *Journal of The Royal Society Interface* **14**, 20170065 (2017).

5 Brokaw, C. J. Flagellar Movement: A Sliding Filament Model: An explanation is suggested for the spontaneous propagation of bending waves by flagella. *Science* **178**, 455-462 (1972).

6 Riedel-Kruse, I. H., Hilfinger, A., Howard, J. & Jülicher, F. How molecular motors shape the flagellar beat. *HFSP journal* **1**, 192-208 (2007).

7 Lindemann, C. B. A" geometric clutch" hypothesis to explain oscillations of the axoneme of cilia and flagella. *Journal of theoretical biology* **168**, 175-189 (1994).

8 Ishijima, S., Hamaguchi, M. S., Naruse, M., Ishijima, S. & Hamaguchi, Y. Rotational movement of a spermatozoon around its long axis. *Journal of experimental biology* **163**, 15-31 (1992).

9 David, G., Serres, C. & Jouannet, P. Kinematics of human spermatozoa. *Gamete research* **4**, 83-95 (1981).

10 Mortimer, S. A critical review of the physiological importance and analysis of sperm movement in mammals. *Human Reproduction Update* **3**, 403-439, doi:10.1093/humupd/3.5.403 (1997).